INTERNATIONAL JOURNAL FOR NUMERICAL METHODS IN FLUIDS
Int. J. Numer. Meth. Fluids **29**: 59–74 (1999)

PARTICLE-TRACKING WITHIN TURBULENT CYLINDRICAL ELECTROMAGNETICALLY-DRIVEN FLOW

S. MCKEE[a,*], R. WATSON[a], J.A. CUMINATO[b] AND P. MOORE[c]

[a] *Department of Mathematics, University of Strathclyde, Glasgow, UK*
[b] *ICMSC-USP University of São Paulo, São Carlos, Brazil*
[c] *Teeside Technology Centre, British Steel, Middlesbrough, UK*

SUMMARY

This paper discusses a simple model of electromagnetically stirred molten metal within a long cylinder, neglecting end effects. The radially-dependent velocity profiles of the molten metal are calculated using the Prandtl mixing length model for turbulence. The paths of non-conducting particles within the fluid are also computed numerically, under the influence of Stokes' drag and a random force due to turbulence. The paths are calculated for a range of particle diameters and the general motion is observed. Copyright © 1999 John Wiley & Sons, Ltd.

KEY WORDS: particle tracking; electromagnetically stirred flows; turbulence; Prandtl mixing length; inclusions

1. INTRODUCTION

The motion of impurities such as silica or aluminium within molten steel is of major interest to the steel industry. The impurities occur in the form of inclusion particles, usually of a lower density than the steel itself (e.g. density of steel $\rho_f = 7200$ kg m^{-3}, density of typical inclusion particle $\rho_p = 2500$ kg m^{-3}). These inclusion particles, if they were to remain within the bulk molten metal, would lead to a degradation in the quality of the resulting steel: it is therefore vital that they are removed. Before this can be done it is necessary to understand their general motion.

The ability to track the paths of any impurities, especially within turbulent flow regimes, is therefore important. Areas of impurity deposition or likely collection points for the removal of said impurities can be ascertained from a statistical analysis of the paths of a large sample of particles.

The problem considered in this paper is a variation on the two-dimensional cylindrical flow model studied by Moffatt [1] and refined in further papers (e.g. References [2–4]). A useful overview of the development of this model is given in Reference [5] (see also References [16–20]). The particular application for this model (the removal of impurities) was studied for liquid sodium by Hayes *et al.* [6] and applied to steel by Marr [7]. More recently, Spitzer *et al.* [8] and Spitzer and Schwerdtfeger [9] discuss a mathematical model for the three-dimensional

---

* Correspondence to: Department of Mathematics, University of Strathclyde, Livingstone Tower, 26 Richmond Street, Glasgow G1 IXH, UK.

CCC 0271–2091/99/010059–16$17.50

electromagnetic stirring which involved Maxwell's equations and $k-\epsilon$ turbulent Navier–Stokes equations: essentially the solution involves a decoupling of the equations. Sazhin *et al.* [10] point out how a conventional computational fluid dynamics code (they principally had FLUENT in mind) could be employed to solve magnetohydrodynamics problems and illustrate this fact for Poiseuille–Hartmann flow.

The configuration is displayed in Figure 1. With such a configuration it will be shown that particle inclusions will be swept towards the centre. These particles may then coagulate and float out, or be removed by some mechanical method. These possibilities are currently under investigation in a number of metal industries. The pole pairs oscillate in value in order to produce a near-continuous rotating sinusoidal magnetic field at the boundary of the circle. For this analysis, the continuity of the field will be assumed.

The following assumptions are made for the particle: the change in velocity over the particle diameter is negligible (i.e. it can be modelled as a point mass) and the particle carries no charge, so that the major forces acting upon the particle arise from Stokes' drag and a pseudo-buoyancy force resulting from the pressure within the fluid. The particles are disperse and small (no more than a few 100 microns) and so they may be assumed neither to act upon the surrounding fluid nor with each other.

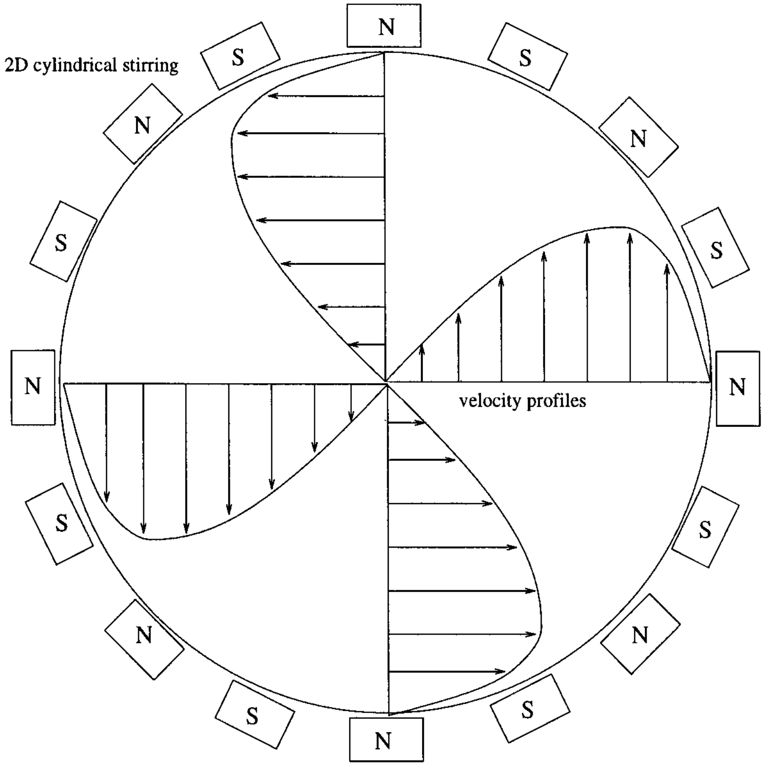

Figure 1. Typical velocity profiles induced by a continuous sinusoidal magnetic field distribution. The number of pole pairs is determined by the parameter m (i.e. in this case $m=8$).

2. ELECTROMAGNETIC FORMULAE

The rate of oscillation of the dipoles determines the angular velocity ω of the boundary field; following Moffatt [1] it is assumed that, in cylindrical polars

$$\vec{B}(a, \theta, z) = (-B_0 \sin(m\theta - \omega t),\ -B_0 \cos(m\theta - \omega t), 0),$$

at $r = a$. Here t denotes time and m the number of pole pairs.

Since the problem is two-dimensional, it is appropriate to work in terms of the vector potential $\vec{A} = (0, 0, A)$ in (r, θ, z) co-ordinates, i.e. the components of $\vec{B}$ are reproducible by the appropriate derivatives of a single-component vector potential. The vector potential itself is represented as

$$A = Re[(A_1 + iA_2)\, e^{i(m\theta - \omega t)}] = A_1 \cos(m\theta - \omega t) - A_2 \sin(m\theta - \omega t), \tag{1}$$

where A_1, A_2 are, respectively, the real and imaginary parts of A.

The appropriate form for Maxwell's equations in cylindrical polar co-ordinates is

$$\vec{B} = \nabla \times \vec{A} = \frac{1}{r}\frac{\partial A}{\partial \theta}\,\hat{\mathbf{r}} - \frac{\partial A}{\partial r}\,\hat{\boldsymbol{\Theta}}, \tag{2}$$

$$\vec{j} = \sigma(\vec{E} + \vec{u} \times \vec{B}), \tag{3}$$

$$\nabla \times \vec{B} = \mu_0 \vec{j}, \tag{4}$$

$$\nabla \times \vec{E} = -\frac{\partial \vec{B}}{\partial t}, \tag{5}$$

$$\nabla \cdot \vec{B} = 0, \tag{6}$$

where the fluid velocity $\vec{u} = (0, u_\theta, 0)$, σ is the conductivity of the fluid, and μ_0 is the permeability of free space. The current density within the fluid is denoted by $\vec{j}$, and $\vec{E}$ and $\vec{B}$ are the electric field intensity and the magnetic flux density respectively; $\hat{\mathbf{r}}$, $\hat{\boldsymbol{\Theta}}$ and $\hat{\mathbf{z}}$ are the unit vectors for the (r, θ, z) directions.

Using Equations (3)–(6), $\vec{E}$ can be eliminated to obtain the governing equation in terms of $\vec{u}$ and $\vec{B}$ only:

$$\frac{\partial \vec{B}}{\partial t} = \nabla \times (\vec{u} \times \vec{B}) + \frac{1}{\mu_0 \sigma} \nabla^2 \vec{B}.$$

From the definition of the vector potential $\vec{B} = \nabla \times \vec{A}$, and the gauge condition $\nabla \cdot \vec{A} = 0$, we obtain

$$\frac{\partial \vec{A}}{\partial t} = \vec{u} \times (\nabla \times \vec{A}) + \frac{1}{\mu_0 \sigma} \nabla^2 \vec{A}, \tag{7}$$

where the vector potential of integration has been shown to be zero by Shercliff [11].

At this point it is convenient to introduce the new variables $\phi = \theta - \omega t/m$ and $\tau = t$, which are equivalent to a frame rotating at the same apparent speed as the magnetic field, i.e. at an angular velocity $\Omega = \omega/m$. Then, with the change of variables $t, \theta \rightarrow \tau, \phi$,

$$\frac{\partial}{\partial t} \equiv \frac{\partial \phi}{\partial t}\frac{\partial}{\partial \phi} + \frac{\partial \tau}{\partial t}\frac{\partial}{\partial \tau} \equiv -\Omega \frac{\partial}{\partial \phi} + \frac{\partial}{\partial \tau},$$

where in this steady frame the time derivative $\partial/\partial\tau \equiv 0$, and using the fact that $\vec{A} = (0, 0, A)$,

$$\vec{u}\times(\nabla\times\vec{A})=(0,0,\ -\vec{u}\cdot\nabla A)=\left(0,0,\ -\frac{u_\theta}{r}\frac{\partial A}{\partial\phi}\right).$$

Equation (7) becomes

$$\nabla^2 A=\mu_0\sigma\left(\frac{u_\theta}{r}-\Omega\right)\frac{\partial A}{\partial\phi}.$$

It is useful to re-write this equation in terms of two non-dimensional parameters—the magnetic Reynolds number $R_{\mathrm{m}}=\mu_0\sigma Ua$ (where U is a typical fluid velocity, a is the radius of the container) and the shielding parameter $R_\omega=\mu_0\sigma\Omega a^2$. These numbers characterise the flow by showing the interaction of the fluid velocity and the magnetic field on flow solutions. After scaling $\tilde{u}=u_\theta/U$, $\tilde{r}=r/a$ the equation becomes

$$\tilde{\nabla}^2 A=\frac{\partial A}{\partial\tilde{r}^2}+\frac{1}{\tilde{r}}\frac{\partial A}{\partial\tilde{r}}+\frac{1}{\tilde{r}^2}\frac{\partial^2 A}{\partial\theta^2}=R_{\mathrm{m}}\frac{\tilde{u}}{\tilde{r}}\frac{\partial A}{\partial\phi}-R_\omega\frac{\partial A}{\partial\phi}. \tag{8}$$

When $R_{\mathrm{m}}\ll R_\omega$, the velocity-based part of the Lorentz force is negligible and the Navier–Stokes equations decouple from Maxwell's equations. However, for the centrifuge problem, flow can be induced within the fluid with angular velocities comparable with the moving magnetic field, so that both terms must be retained.

Equation (8) can be expressed as the following system of equations:

$$\frac{\partial^2 A_1}{\partial r^2}+\frac{1}{r}\frac{\partial A_1}{\partial r}-\frac{m^2}{r^2}A_1=a^2\mu_0\sigma\left(\omega-\frac{mu_\theta}{r}\right)A_2, \tag{9a}$$

$$\frac{\partial^2 A_2}{\partial r^2}+\frac{1}{r}\frac{\partial A_2}{\partial r}-\frac{m^2}{r^2}A_2=-a^2\mu_0\sigma\left(\omega-\frac{mu_\theta}{r}\right)A_1, \tag{9b}$$

where A_1 and A_2 are the real and imaginary parts of the vector potential relation shown in Equation (1), and the tilde has been omitted for clarity.

3. FLUID FLOW FORMULAE

In cylindrical polar co-ordinates (r,θ,z) the Navier–Stokes equations are

$$\frac{\partial\vec{u}}{\partial t}+(\vec{u}\cdot\nabla)\vec{u}=-\frac{1}{\rho_f}\nabla p+\nabla\cdot(\eta\nabla\vec{u})+\vec{F}, \tag{10}$$

and the continuity equation is

$$\frac{1}{r}\frac{\partial}{\partial r}(ru_r)+\frac{1}{r}\frac{\partial u_\theta}{\partial\theta}+\frac{\partial u_z}{\partial z}=0, \tag{11}$$

where $\vec{u}=(u_r,u_\theta,u_z)$ and $\vec{F}$ is the body force per unit mass driving the fluid motion.

In the two-dimensional centrifuge application, the θ- and z-derivatives are negligible and $\vec{u}=(0,u_\theta,0)$. In this case, Equation (11) is automatically satisfied, and only the radially-dependent component of Equation (10) need be considered.

The azimuthal form of the time-averaged Navier–Stokes equation for this problem is

$$\eta\frac{\partial^2 u_\theta}{\partial r^2}+\left(\frac{\eta}{r}+\frac{\partial\eta}{\partial r}\right)\frac{\partial u_\theta}{\partial r}-\left(\frac{\eta}{r^2}-\frac{1}{r}\frac{\partial\eta}{\partial r}\right)u_\theta=\frac{1}{\rho_f}\langle\vec{j}\times\vec{B}\rangle_\theta, \tag{12}$$

where, for a fluid density, ρ_f, $\langle \vec{j} \times \vec{B} \rangle_\theta / \rho_f$ is the time-averaged Lorentz force driving the flow in the θ-direction and η is the viscosity of the fluid. The pressure is radially-dependent and the radial pressure gradient is given by the radial component of the Navier–Stokes equation

$$\frac{\partial p}{\partial r} = \rho_f \frac{u_\theta^2(r)}{r}. \tag{13}$$

To incorporate the Prandtl mixing length model for turbulence, η must be modified by the additional turbulence viscosity η_{t}, which is a function of the radial distance r,

$$\eta = \eta_0 + \eta_{\mathrm{t}}(r) = \eta_0 + l^2 \left| \frac{\partial u_\theta}{\partial r} - \frac{u_\theta}{r} \right|, \tag{14}$$

where l is the mixing length parameter with the experimental value 0.003 m (see e.g. Reference [12]).

The Prandtl mixing length model is the simplest of the modified viscosity models. It is isotropic, so it will fail to take any anisotropic turbulence into account which will exist at a wall surface and may exist due to the electromagnetic induction. Even some of the more advanced models, such as the $k - \epsilon$ and $k - w$ models share its restriction. In order to account for anisotropy it would be necessary to use either the algebraic stress, or full Reynolds stress models. These would require considerably more computation and any electromagnetic induced turbulence would have to be incorporated, thus modifying these basic equations.

Thus Equation (12) becomes

$$(1 + \alpha) \frac{\partial^2 u_\theta}{\partial r^2} + \left(\frac{1 + \alpha}{r} + \frac{\partial \alpha}{\partial r} \right) \frac{\partial u_\theta}{\partial r} - \left(\frac{1 + \alpha}{r^2} - \frac{1}{r} \frac{\partial \alpha}{\partial r} \right) u_\theta = \frac{\langle \vec{j} \times \vec{B} \rangle_\theta}{\eta_0 \rho_f}, \tag{15}$$

where $\alpha(r) = \eta_{\mathrm{t}}/\eta_0 = l^2 |(\partial u_\theta / \partial r) - (u_\theta / r)| / \eta_0$.

The time-averaged Lorentz force in the θ-direction is

$$\begin{aligned}
\langle \vec{j} \times \vec{B} \rangle_\theta &= \langle \sigma(\vec{E} + \vec{u} \times \vec{B}) \times \vec{B} \rangle_\theta = \left\langle \sigma\left(-\frac{\partial \vec{A}}{\partial t} + \vec{u} \times (\nabla \times \vec{A}) \right) \times (\nabla \times \vec{A}) \right\rangle_\theta \\
&= \frac{\omega}{2\pi} \int_0^{2\pi/\omega} \left(-\sigma\left[\left(\frac{\partial A}{\partial t} + \frac{u_\theta}{r} \frac{\partial A}{\partial \theta} \right) \hat{\mathbf{z}} \right] \times \left[\frac{1}{r} \frac{\partial A}{\partial \theta} \hat{\mathbf{r}} - \frac{\partial A}{\partial r} \hat{\mathbf{\Theta}} \right] \right)_\theta \mathrm{d}t \\
&= \frac{\omega}{2\pi} \int_0^{2\pi/\omega} \left(\frac{\sigma}{r} \frac{\partial A}{\partial \theta} \left[\frac{\partial A}{\partial t} + \frac{u_\theta}{r} \frac{\partial A}{\partial \theta} \right] \right) \mathrm{d}t.
\end{aligned} \tag{16}$$

Noting, from Equation (1), that

$$\frac{\partial A}{\partial \theta} = -m(A_1 \sin(m\theta - \omega t) + A_2 \cos(m\theta - \omega t)),$$

and

$$\frac{\partial A}{\partial t} = \omega(A_1 \sin(m\theta - \omega t) + A_2 \cos(m\theta - \omega t)),$$

this time-averaged body force component can be written as

$$\begin{aligned}
\langle \vec{j} \times \vec{B} \rangle_\theta &= \frac{\sigma}{r} \frac{\omega}{2\pi} \int_0^{2\pi/\omega} \left(-m\omega + m^2 \frac{u_\theta}{r} \right) [A_1 \sin(m\theta - \omega t) + A_2 \cos(m\theta - \omega t)]^2 \, \mathrm{d}t \\
&= \frac{m\sigma}{r} \left(\frac{m u_\theta}{r} - \omega \right) \frac{\omega}{2\pi} \int_0^{2\pi/\omega} [A_1^2 \sin^2(m\theta - \omega t)] \, \mathrm{d}t
\end{aligned}$$

$$
\begin{aligned}
&+\frac{m\sigma}{r}\left(\frac{mu_\theta}{r}-\omega\right)\frac{\omega}{2\pi}\int_0^{2\pi/\omega}[2A_1A_2\sin(m\theta-\omega t)\cos(m\theta-\omega t)]\,\mathrm{d}t\\
&+\frac{m\sigma}{r}\left(\frac{mu_\theta}{r}-\omega\right)\frac{\omega}{2\pi}\int_0^{2\pi/\omega}[A_2^2\cos^2(m\theta-\omega t)]\,\mathrm{d}t\\
&=\frac{m\sigma}{r}\left(\frac{mu_\theta}{r}-\omega\right)\frac{\omega}{2\pi}\int_0^{2\pi/\omega}\frac{A_1^2+A_2^2}{2}\,\mathrm{d}t+\frac{m\sigma}{r}\left(\frac{mu_\theta}{r}-\omega\right)\frac{\omega}{2\pi}\int_0^{2\pi/\omega}A_1A_2\sin 2(m\theta-\omega t)\,\mathrm{d}t\\
&+\frac{m\sigma}{r}\left(\frac{mu_\theta}{r}-\omega\right)\frac{\omega}{2\pi}\int_0^{2\pi/\omega}\frac{A_2^2-A_1^2}{2}\cos 2(m\theta-\omega t)\,\mathrm{d}t\\
&=-\frac{m\sigma}{2r}\left(\omega-\frac{mu_\theta}{r}\right)(A_1^2+A_2^2).
\end{aligned}
\tag{17}
$$

Note that in Equation (17) the strength of the force is partly determined by the relative difference between the angular velocity of the travelling magnetic field ω and that of the fluid flow mu_θ/r. Thus, in some regimes, the force can act as a break so that the flow does not outstrip the magnetic field.

The fluid flow is thus determined by the joint equations (9) and the combination of Equations (14) and (15), linked by the Lorentz force through Equation (17). A numerical scheme is derived which gives approximate values of α, u_θ, A_1 and A_2 as functions of r.

4. NUMERICAL SCHEME FOR DETERMINATION OF $u_\theta(r)$

The problem is non-dimensionalised by scaling the radial direction on the radius of the cylinder, so that $r=1$ and $r=-1$ are the boundaries for the numerical problem. The interval $[-a, a]$ is split into an odd number of grid cells N in order to avoid the singularities of $1/r$ and $1/r^2$ at $r=0$.

The variables A_1, A_2 and u_θ are discretised at each of the nodal points i, $i=0,\dots,N$ as $A_1^{(i)}, A_2^{(i)}$ and $U^{(i)}$. The derivatives are approximated by the standard central difference approximations, e.g. for $U^{(i)}$, $i\neq 0$, N:

$$
\frac{\partial^2 U^{(i)}}{\partial r^2}\approx\frac{U^{(i+1)}-2U^{(i)}+U^{(i-1)}}{\Delta^2},\qquad \frac{\partial U(i)}{\partial r}\approx\frac{U^{(i+1)}-U^{(i-1)}}{2\Delta},
$$

where $\Delta=2a/N$, with similar formulae for A_1 and A_2.

The turbulence parameter α is obtained from the values $U^{(i)}$ via the discretisation

$$
\alpha^{(i)}=\frac{l^2}{\eta_0}\left|\left(\frac{U^{(i+1)}-U^{(i-1)}}{2\Delta}\right)-\left(\frac{U^{(i)}}{i\Delta-1}\right)\right|.
\tag{18}
$$

A similar approximation is made for the derivative of $\alpha^{(i)}$ as was made above for $\partial U^{(i)}/\partial r$.

4.1. Boundary conditions

At the boundary, the usual no-slip conditions are applied to the velocity, i.e. $U^{(0)}=U^{(N)}=0$. The turbulent viscosity parameter α is set equal to zero at the boundaries, i.e. the viscosity at the boundary is given the value η_0.

The magnetic vector potential boundary conditions are derived from the form of the travelling magnetic field. From Equation (2),

$$\vec{B} = \nabla \times \vec{A} = \frac{1}{r}\frac{\partial A}{\partial \theta}\,\hat{\mathbf{r}} - \frac{\partial A}{\partial r}\,\hat{\mathbf{\Theta}}, \tag{19}$$

and at $r = a$, $\vec{B}(r, \theta, z) := \vec{B}(a, \theta) = (-B_0 \sin(m\theta - \omega t),\ -B_0 \cos(m\theta - \omega t), 0)$, implying that

$$\frac{\partial A}{\partial r} = B_0 \cos(m\theta - \omega t),$$

and so, referring back to Equation (1), at $r = a,\ -a$ the boundary conditions for A_1 and A_2 are

$$\frac{\partial A_1}{\partial r} = B_0, \qquad \frac{\partial A_2}{\partial r} = 0.$$

Equations (9), (12) and (14) are discretised with the standard central difference formulae shown earlier. The coupled system derived from Equation (9) is solved initially to machine precision by the application of a standard Gauss–Seidel solver. If the values of A_1 and A_2 are assumed to be independent of the velocity u_θ (i.e. if the frequency of the magnetic field is sufficiently large), then this system need only be solved once. Clearly a more sophisticated iterative solver could have been employed. However, the problem is only one-dimensional and computational speed is not of the essence.

The Lorentz force from Equation (17) is then substituted into the numerical system based on the discretisation of Equation (15). As an initial starting solution, all the α_i are set to zero and the system is solved by employing a standard Gauss–Seidel numerical method without the turbulence parameters. These initial values are used as the starting point for the fully-turbulent solution, again using Gauss–Seidel.

The cases where the fluid velocity couples with the vector potential require that the system based on Equation (9) be updated after a fixed number of velocity iterations. A_1 and A_2 are again solved to machine precision and the updated Lorentz force inserted into the velocity equations. This cycle is repeated until the residuals of A_1, A_2 and u_θ all reach prescribed lower limits (machine precision if possible). Velocity profiles for differing values of ω and m or increasing B_0 are shown in Figures 2, 4 and 5. The effect of frequency on the values of A_1 and A_2 is shown in Figure 3.

The turbulence parameters are also graphed in Figures 6 and 7, showing the dependence of frequency and number of pole pairs in the creation of turbulent flow.

5. PARTICLE TRACKING

In cylindrical polar co-ordinates the velocity $\vec{v}$ and acceleration $\vec{a}$ of a particle at the point (r, θ, z) are given by

$$\vec{v} = r'\hat{\mathbf{r}} + r\theta'\hat{\mathbf{\Theta}} + z'\hat{\mathbf{z}}, \tag{20a}$$

$$\vec{a} = (r'' - r(\theta')^2)\hat{\mathbf{r}} + (r\theta'' + 2r'\theta')\hat{\mathbf{\Theta}} + z''\hat{\mathbf{z}}, \tag{20b}$$

where the dashes denote derivatives with respect to time t.

The fluid velocity profiles computed in the previous section are linked to a radial pressure gradient through the radial component of the Navier–Stokes equation:

$$\frac{\partial p}{\partial r} = \rho_f \frac{u_\theta^2(r)}{r}. \tag{21}$$

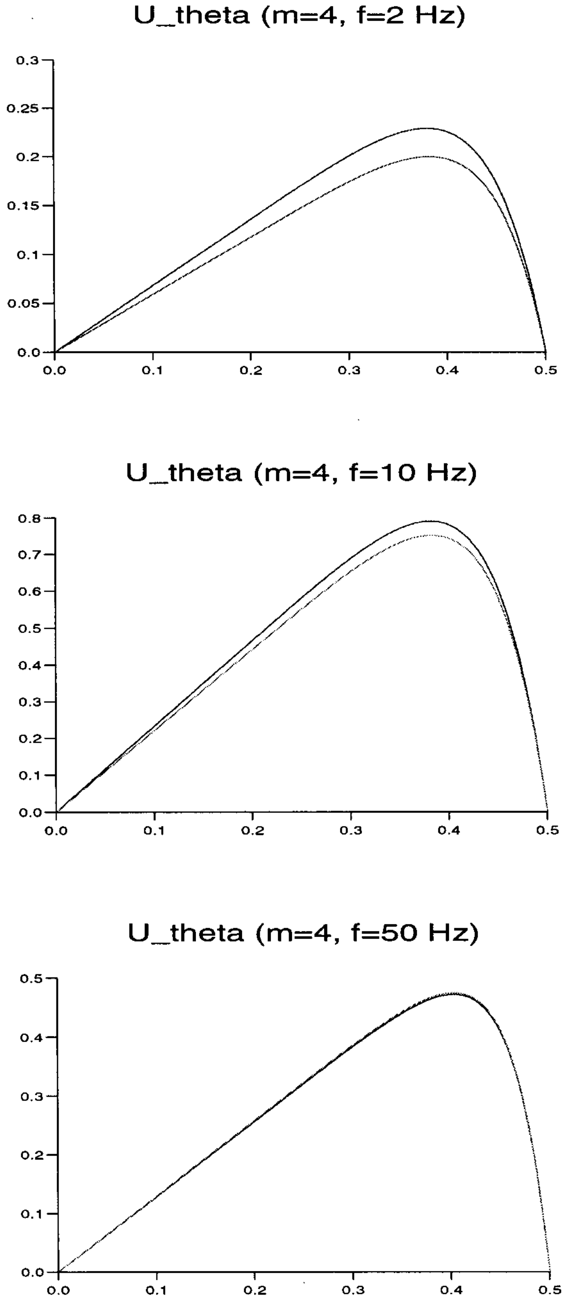

Figure 2. Fluid velocity profiles for fixed number of pole pairs and varying frequency ($B_0 = 0.001$ T) versus radial distance ($a = 0.5$ m). In each picture the velocity has been calculated both for a velocity-coupled Lorentz force and for an uncoupled force. At lower frequencies the disparity between the two is more pronounced (the lower-valued velocity profiles are the coupled cases), whilst at higher frequencies the difference is negligible.

This pressure gradient gives rise to a pseudo-buoyancy force whereby a spherical particle displacing its own volume ($\pi d^3/6$, where d is the diameter of the particle) of fluid experiences a force in the radial direction, equal to

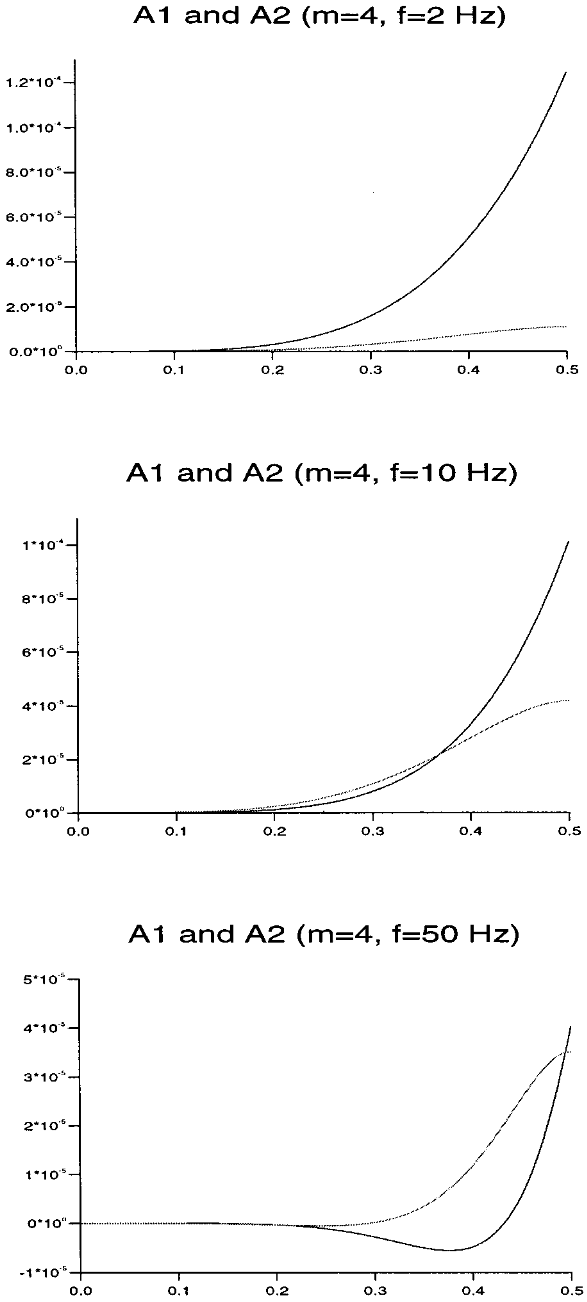

Figure 3. Real and imaginary parts of A, the vector potential for varying frequency ($B_0 = 0.001$ T) versus radial distance ($a = 0.5$ m). At higher frequencies the imaginary part becomes more dominant (the imaginary part in all three pictures has a zero-valued gradient at $r = 0.5$ m).

$$\vec{F}_{\mathrm{b}} = -\frac{\pi d^3}{6}\rho_f \frac{u_\theta^2(r)}{r}\,\hat{\mathbf{r}}. \tag{22}$$

The other force which determines the particle behaviour is the Stokes' drag, which acts to decrease the relative velocity between the particle and the surrounding fluid:

$$\vec{F}_s = -3\pi d\rho_f\eta(r'\hat{\mathbf{r}} + (r\theta' - u_\theta(r))\hat{\mathbf{\Theta}} + z'\hat{\mathbf{z}}). \tag{23}$$

In the z-direction the force of gravity acts and is counter-balanced to some extent by the natural buoyancy force imparted to the particle by the fluid.

In component form the following system of equations is obtained:

$$\frac{\pi d^3}{6}\rho_p(r'' - r(\theta')^2) = -3\pi d\rho_f\eta r' - \frac{\pi d^3}{6}\rho_f\frac{u_\theta^2(r)}{r}, \tag{24a}$$

$$\frac{\pi d^3}{6}\rho_p(r\theta'' + 2r'\theta') = -3\pi d\rho_f\eta(r\theta' - u_\theta(r)), \tag{24b}$$

$$\frac{\pi d^3}{6}\rho_p z'' = -3\pi d\rho_f\eta z' + (\rho_f - \rho_p)\frac{\pi d^3}{6}g. \tag{24c}$$

It should be noted that these equations are only valid for small particle Reynolds numbers. A more sophisticated approach, employed by Morsi and Alexander [13], was to fit the drag coefficient to a function of the particle Reynolds number so that agreement with experiments was uniformly within at most 2%.

In Equation (24c), the value of g is taken to be 9.81 m s^{-2}. The velocity for the z-direction is given by

$$z' = v_0\,\mathrm{e}^{((-18/d^2)(\rho_f/\rho_p)(\eta t))} + \frac{d^2 g}{18\eta}\left(1 - \frac{\rho_p}{\rho_f}\right)(1 - \mathrm{e}^{((-18/d^2)(\rho_f/\rho_p)(\eta t))}),$$

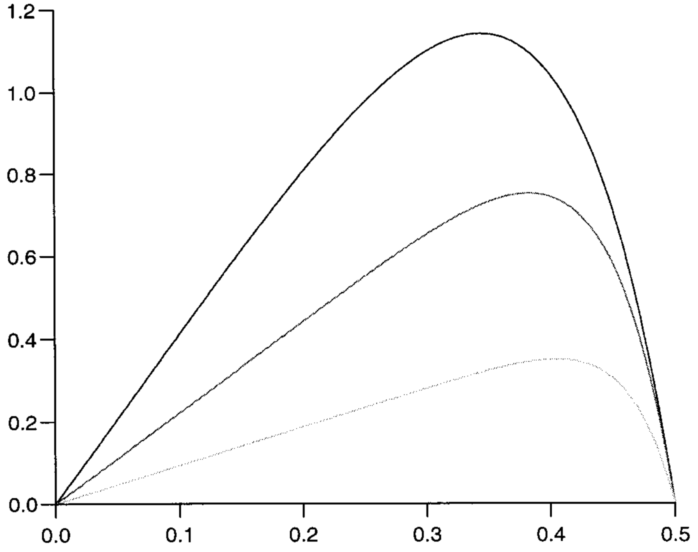

Figure 4. Fluid velocity profiles for fixed frequency and varying number of pole pairs $m = 2$, 4, 6 versus radial distance ($a = 0.5$ m), with $B_0 = 0.001$ T. As the number of pole pairs increases, the relative frequency of the magnetic field (ω/m) decreases, giving smaller angular velocities in the fluid.

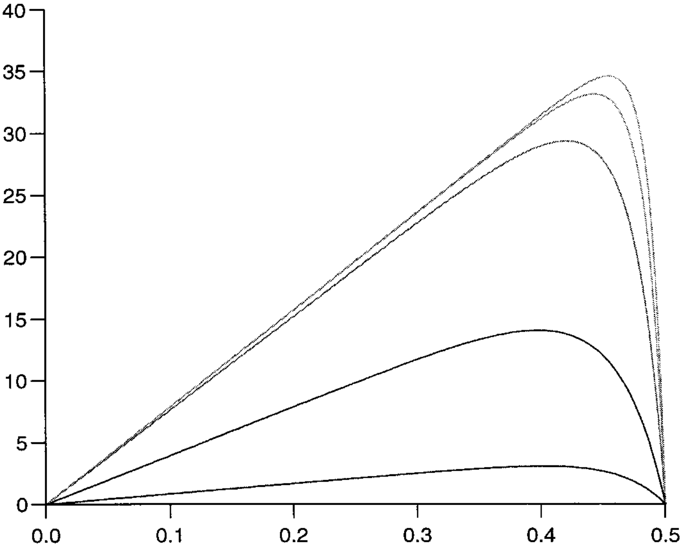

Figure 5. Graphs of the fluid velocities at $m = 4$, $\omega = 100\pi\ \mathrm{s}^{-1}$ with $B_0 = 2.5$, 5.0, 7.5, 10.0, 12.5×10^{-3} T against radial distance ($a = 0.5$ m). The increase in field strength increases the velocity, yet there remains an upper bound, limited by the frequency of the magnetic field (i.e. the Lorentz force tends to zero over most of the radial distance when $u_\theta(r)$ approaches $\omega r/m$).

where v_0 is the initial velocity of the particle in the z-direction. The particle tends towards a terminal velocity in the z-direction of value

$$v_t \frac{d^2g}{18\eta}\left(1-\frac{\rho_p}{\rho_f}\right),$$

which is either positive or negative depending on the relative values of ρ_p and ρ_f (this holds true so long as the particle remains in a region where the turbulence is negligible, i.e. the central rotating core).

Since the z-component decouples easily, it only remains to solve the other components in tandem. Dividing throughout by $\pi d^3\rho_p/6$, then give

$$r'' - r(\theta')^2 = -18\frac{\rho_f\eta}{\rho_p d^2}r' - \frac{\rho_f}{\rho_p}\frac{u_\theta^2(r)}{r}, \tag{25a}$$

$$r\theta'' + 2r'\theta' = -18\frac{\rho_f\eta}{\rho_p d^2}(r\theta' - u_\theta(r)). \tag{25b}$$

Setting $X_1 = r$, $X_2 = \theta'$ and $X_3 = r'$ the system can be transformed into a suitable form for a Runge–Kutta numerical solver, i.e.

$$X_1' = r' = X_3, \tag{26a}$$

$$X_2' = \theta'' = -18\frac{\rho_f\eta}{\rho_p d^2}\left(X_2 - \frac{u_\theta(X_1)}{X_1}\right) - \frac{2X_2X_3}{X_1}, \tag{26b}$$

$$X_3' = r'' = -18\frac{\rho_f\eta}{\rho_p d^2}X_3 - \frac{\rho_f}{\rho_p}\frac{u_\theta^2(X_1)}{X_1} + X_1(X_2)^2. \tag{26c}$$

A fourth-order Runge–Kutta solver is applied to the system of Equations (26) in order to calculate r, θ' and r' at times $t_i = i\Delta t$.

5.1. Random perturbations to particle motion

An additional perturbation to the particle path was added with the introduction of random forces due to turbulence.

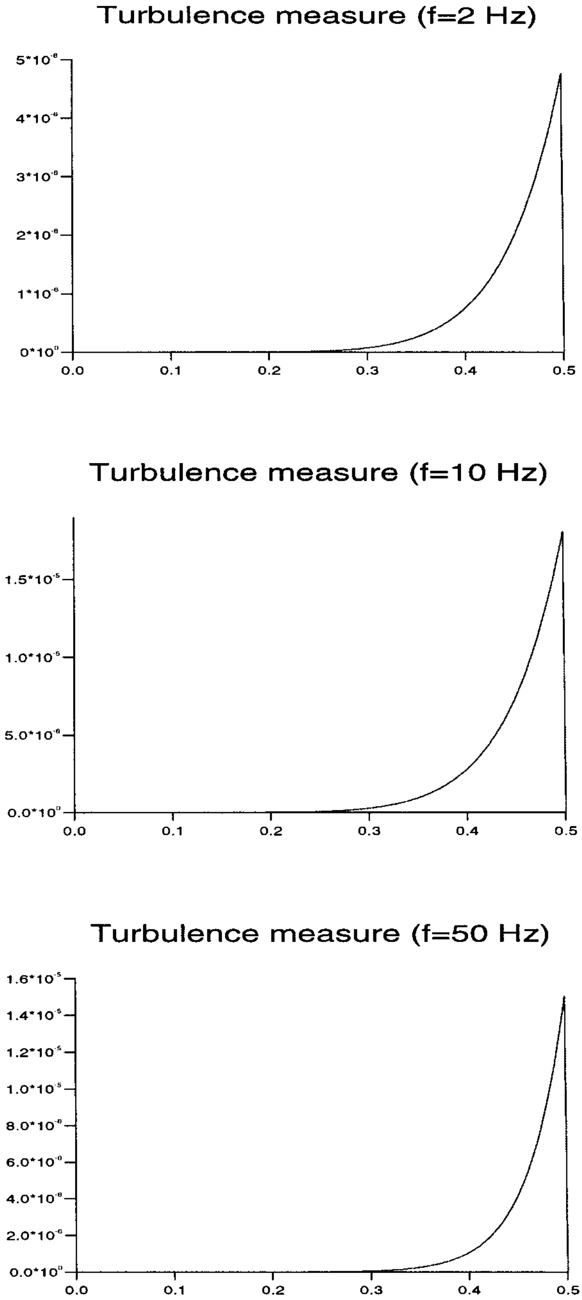

Figure 6. Graphs of α/l^2 versus radial distance for $m=4$, frequency = 2, 10, 50 Hz. All three graphs demonstrate that the turbulence effects are at their greatest close to the walls. Note that the peak of the turbulence measure decreases for larger frequencies.

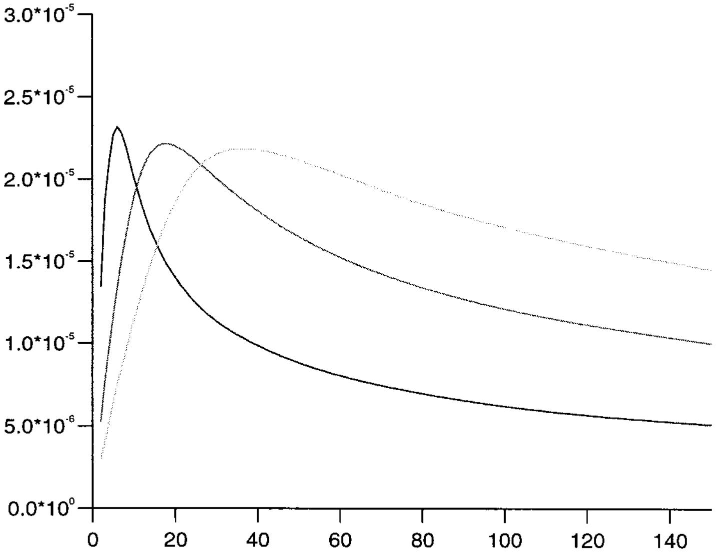

Figure 7. Graphs of the maximum attained values of α/l^2 versus frequency for $m = 2$, 4, 6. The peak frequency at which the turbulence parameter attains a maximum increases with the number of pole pairs, and the decay rate is also proportionally weaker.

Following Bush [14], additional velocities of the order of

$$v_p = C_1\left(\frac{4}{3}k\right)^{1/2},$$

were added to the particle velocity to simulate the effects of turbulent eddies with the turbulent kinetic energy k; C_1 is a normally distributed random number in the range [0, 1] and the angle of this additional velocity component was uniformly distributed over $[0, 2\pi]$.

Once the particle had travelled a distance equal to $l_t = \eta_t/k^{1/2}$, the additional random velocity component was re-calculated and substituted for the previous additional value. The kinetic energy k was given the experimental value of 2×10^{-5} m^2 s^{-2}.

To accomplish this, the estimated lengths of the particle path from the previous additional eddy was calculated via

$$(\Delta s)^2 \approx (r'\Delta t)^2 + (r\theta'\Delta t)^2,$$

so that by noting

$$s = \Delta t \sum_{i=1}^{n} \sqrt{(X_3^{(i)})^2 + (X_1^{(i)}X_2^{(i)})^2}, \tag{27}$$

and stopping at the value of the step number n at which s exceeds l_t, the next eddy effect could then be calculated.

The resultant particle trajectories for different sizes of particles are displayed in Figure 8.

6. RESULTS AND CONCLUSIONS

This work has been primarily concerned with determining the paths of non-conducting particles within electromagnetically stirred molten metal in a large cylinder under the influence

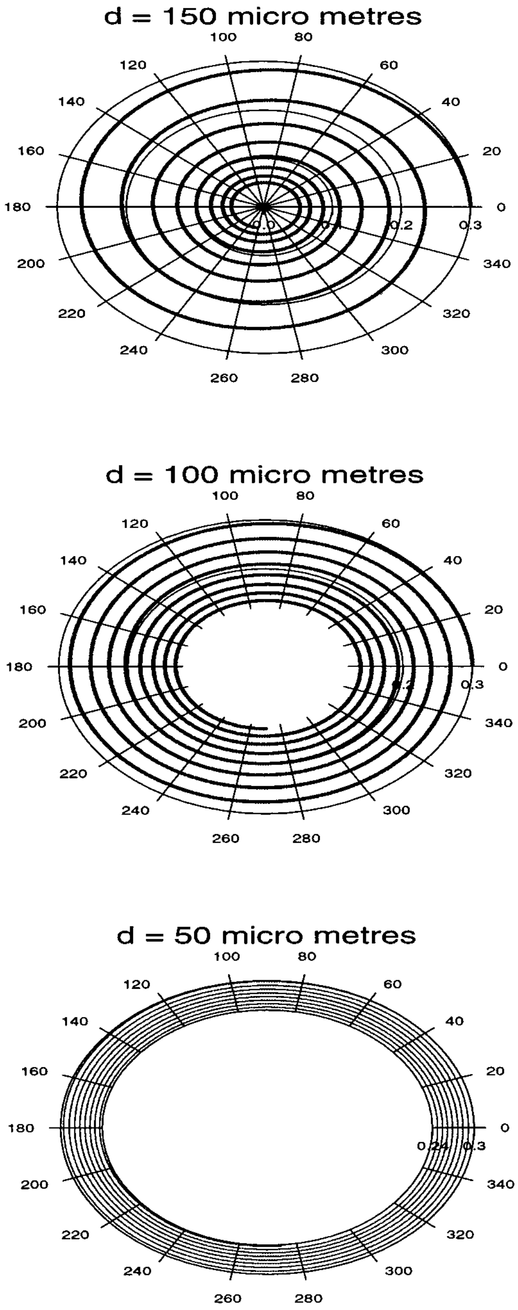

Figure 8. Particle tracks for particle diameters of 150, 100 and 50 μm, respectively. The time at which each simulation was stopped is 1 s, to give an impression of the relative rates of progress towards the centre. Each particle was released at $r = 0.3$ m with no initial angular or radial velocity. The fluid velocity field that each particle was subjected to was calculated for the parameters: $B_0 = 7.5 \times 10^{-3}$ T, two pole pairs, frequency = 50 Hz.

of Stokes' drag and a random force due to turbulent fluctuations. The molten metal was driven by pole pairs which were allowed to oscillate in value in order to produce a nearly continuous rotating sinusoidal magnetic field at the cylinder. The radial-dependent velocity profiles of the molten metal were calculated using the Prandtl mixing length model for turbulence.

Before computing the particle paths the fluid velocity profiles were determined for a number of pole pairs and frequencies. As anticipated, a boundary layer formed close to the wall of the cylinder ($r = a$) displaying maximum velocity in the region close to the walls. As the frequency decreased from 50 Hz the maximum velocity increased before again decreasing. The calculation was performed both for the velocity-coupled Lorenz force and the uncoupled force. At 50 Hz it was observed that there was little difference, but at 2 Hz (the case of interest for British Steel) the two solutions differed by $\approx 20\%$ indicating the need to solve the coupled system.

Velocity profiles were also calculated for a fixed frequency and a varying number of pole pairs. In this case we observed that as the number of pole pairs increased, the relative frequency of the magnetic field decreased, giving rise to substantially smaller angular velocities in the fluid. Fluid velocities were also computed for a number of different field strengths for four pole pairs. Not surprisingly, an increase in field strength displayed an increase in fluid velocity. However, above $B_0 = 7.5 \times 10^{-3}$ T, an asymptotic maximum velocity was soon attained.

In addition, a turbulence measure ($\alpha/l^2 = (\eta_t/\eta_0)/l^2$) was plotted against radial distance for a range of frequencies, showing that turbulence effects were greater near the walls and decreased with increasing frequencies. The maximum value of α/l^2 was plotted against frequency for different pole pairs. It was noted that the maximum value attained by the turbulence parameter increased with increasing pole pairs.

Before computing the particle trajectories, random perturbations were added to the particle motion and typical particle tracks were plotted for different particle diameters (see Figure 8). It was observed that the smaller (i.e. the lighter) the particles the longer it took to spiral into the centre of the cylinder. The particle paths clearly display the centripetal force imparted by the fluid flow. The size of the particle determines the rate of progress towards the centre of the cylinder for this simple two-dimensional model, and this is observed in practice in steel production. The random eddies have little or no influence on the larger particles, but for smaller particles the random eddy influence is greater. Smaller particles will therefore tend to be less concentrated at the centre of the cylinder. Study of the possible coagulation of these smaller particles into larger conglomerates would perhaps be of benefit, since these would tend to behave like the larger particles and draw more rapidly towards the centre.

Possible future work could be the extension towards a three-dimensional model along the lines of Davidson [15] to track the particles in both poloidal and meridianal flows.

This work presents an initial first step in understanding quantitatively how non-conducting particles within an electromagnetically stirred turbulent molten metal move, and in particular, how rapidly they tend towards the centre of a cylinder. These inclusion particles must be removed if the quality of the finished steel is to be maintained: an understanding of the particle motion is first essential if an effective collection device is to be designed.

ACKNOWLEDGMENTS

R. Watson would like to acknowledge the encouragement and support afforded by the ESPRC in the form of a studentship.

REFERENCES

1. H.K. Moffatt, 'On fluid flow induced by a rotating magnetic field', *J. Fluid Mech.*, **22**, 521–528 (1965).
2. A.D. Sneyd, 'Generation of fluid motion in a circular cylinder by an unsteady applied magnetic field', *J. Fluid Mech.*, **49**, 817–827 (1971).

3. A.D. Sneyd, 'Fluid flow induced by a rapidly alternating or rotating magnetic field', *J. Fluid Mech.*, **92**, 35–51 (1979).
4. E. Dahlberg, 'On the action of a rotating magnetic field on a conducting liquid', AB Atomenergi Report, AE-477, Sweden, 1972.
5. A.D. Sneyd, 'Theory of electromagnetic stirring by AC fields', *IMA J. Math. Appl. Bus. Ind.*, **5**, 87–113 (1994).
6. D.J. Hayes, M.R. Baum and M.R. Hobdell, 'The performance and applications of an electromagnetic rotary-flow device in liquid sodium', *J. Br. Nucl. Energy Soc.*, **10**, 93–98 (1971).
7. H.S. Marr, 'Electromagnetic stirring in continuous casting of steel', Proc. IUTAM Symp. on Metallurgical Applications of Magnetohydrodynamics, Cambridge, 1984, pp. 143–153.
8. K.-H. Spitzer, M. Dubke and K. Schwerdtfeger, 'Rotational electromagnetic stirring in continuous casting of round strands', *Metall. Trans.*, **17B**, 119–131 (1986).
9. K.-H. Spitzer and K. Schwerdtfeger, 'The magnetic field of inductors used for rotating stirring in the continuous casting of steel', *Trans. ISS*, **17**, 57–71 (1990).
10. S.S. Sazhin, M. Makhlouf and T. Ishii, 'Solutions of magnetohydrodynamic problems based on a conventional computational fluid dynamic code', *Int. J. Numer. Methods Fluids*, **21**, 433–442 (1995).
11. J.A. Shercliff, *A Textbook on Magnetohydrodynamics*, Pergamon Press, Oxford, London, New York, 1965.
12. P. Moore, 'Mathematical modelling of fluid flow in the steel industry', *Ph.D. Thesis*, Teesside Polytechnic, 1987.
13. S.A. Morsi and A.J. Alexander, 'An investigation of particle trajectories in two-phase flow systems', *J. Fluid. Mech.*, **55**, 193–208 (1972).
14. A.W. Bush, B.A. Lewis and M.D. Warren, *Flow Modelling in Industrial Processes*, Ellis Horwood, Chichester, UK, 1989.
15. P.A. Davidson and J.C.R. Hunt, 'Swirling recirculating flow in a liquid-metal column generated by a rotating magnetic field', *J. Fluid Mech.*, **185**, 67–106 (1987).
16. J.M. Galpin and Y. Fautrelle, 'Liquid-metal flows induced by low-frequency alternating magnetic fields', *J. Fluid Mech.*, **239**, 383–408 (1992a).
17. J.M. Galpin, Y. Fautrelle and A.D. Sneyd, 'Parametric resonance in low-frequency magnetic stirring', *J. Fluid Mech.*, **239**, 409–427 (1992b).
18. H.K. Moffatt, 'Rotation of liquid metal under the action of a rotating magnetic field', in H. Branover and A. Yakhot (eds.), *Proc. 2nd Beer-Sheva Seminar on MHD Flows and Turbulence*, Israel, 1980, pp. 65–82.
19. R. Moreau, 'MHD flows driven by alternating magnetic fields', in H. Branover and A. Yakhot (eds.), *Proc. 2nd Beer-Sheva Seminar on MHD Flows and Turbulence*, Israel, 1980, pp. 65–82.
20. R. Moreau, *Magnetohydrodynamics*, Kluwer, Dordrecht, 1994.